Section S1. The free-jet flow-tube experiments.

To minimize wall effects within the flow-tube, achieving laminar flow is essential. However, effective investigation of chemical reactions also requires thorough mixing of oxidants and reactants. Therefore, it is critical to select the total flow rate based on the length and inner diameter of the flow-tube, and to determine the injector flow rate according to the nozzle inner diameter. We adopted the flow-tube and injector design from a well-established free-jet flow system developed by Berndt et al. (2015b, a, 2016), including the same flow rates: 95 L min^{-1} for the main flow and 5 L min^{-1} for the injector. To help the main flow to be laminar before mixing with the injector stream, two stainless-steel meshes were installed to two stainless-steel rings: one near the large flange (fixed) and another supporting (and moving with) the injector (Fig. 1).

Computational fluid dynamics (CFD) simulations were performed using COMSOL Multiphysics (COMSOL, Inc.), including ozonolysis of 2,3-dimethyl-2-butene (TME). The results closely matched those reported by Berndt et al. (2015b): the central flow velocity increases to approximately 15 m s^{-1} at the nozzle and then rapidly decreases. Based on the ozone (O_3) concentration without chemical conversion, the complete mixing along the centerline is achieved around 0.3–0.4 m downstream the nozzle.

Due to the challenges in accurately modeling turbulent mixing, we conducted laminarity tests using smoke to visually assess the flow behavior under experimental conditions (videos are available as archived in Zenodo: https://doi.org/10.5281/zenodo.17250833; Zhang et al., 2025). Smoke was generated using a fluid smoke machine (OPTI MIST, Le Maitre Ltd) and blown at 23 L min^{-1} to mix with 72 L min^{-1} of zero air as the main flow. The tests show that after a thorough turbulent mixing, the flow became laminar approximately 40–50 cm downstream the nozzle.

Based on the smoke tests, we determined that the shortest reaction distance to be used was 50 cm. The effective reaction time was then experimentally determined from a reaction distance from 50 to 110 cm, using ozonolysis of TME (Berndt et al., 2015b). In the presence of excess of TME relative to O_3 ($[O_3]_{max} = 9.5 \times 10^{11}$ cm^{-3}, [TME] = $(0.2 – 1.44) \times 10^{14}$ cm^{-3}), the effective reaction time, t, was calculated using the expression:

$$\frac{[O_3]_{TME}}{[O_3]_0} = exp\left(-[TME] \cdot k_{TME+O_3} \cdot t\right) \quad (S1)$$

assuming constant [TME] and using a rate coefficient of $k_{TME+O3} = 1 \times 10^{11}$ cm^3 $molecule^{-1}$ s^{-1} (Witter et al., 2002). The decay of O_3 was monitored by a photometric O_3 analyzer. After correcting for a 3 s residence time in the sampling line and O_3 analyzer, the effective reaction times at different distances were determined (Fig. S1): 2.5 s (50 cm), 4.6 s (70 cm), 6.4 s (90 cm), and 8.3 s (110 cm).

Compressed air supplied to the zero-air generator (ZA-737-250, Tisch Environmental) was filtered to remove particles and water vapors. After passing through the zero-air generator and mass flow controllers (MKS, Inc.), the main flow was further purified using adsorber containers (IAH-336A, Infiltec GmbH) filled with molecular sieves (9Å, IAC-510B, Infiltec GmbH), followed by HEPA filters (Whatman plc) to ensure particle-free conditions. During our experiments, throughout the flow-tube reaction distance, concentrations of O_3, NO_2, and monoterpenes (MTs) remained nearly constant, with conversion ratio generally below 1%, based on box model simulations (see Fig. S2 for example). Consequently, there was no particle present in our experiments, as the feed gas was particle-free and particle formation did not occur due to the low reactant conversion and short reaction time. This is consistent with earlier flow-tube experiments under similar conditions (Berndt et al., 2018).

Section S2 Instrumentation and quantification

The chemical ionization mass spectrometer (CIMS, Tofwerk AG/Aerodyne Research, Inc.) was coupled with an Eisele-type inlet (Eisele and Tanner, 1993). The sample flow is drawn in through a ¾-inch stainless steel tube at 10 L min^{-1}. A sheath flow is introduced at 20 L min^{-1} to minimize wall losses, and it carries either diethylamine (DEA) or isotopically labeled nitric acid ($H^{15}NO_3$) across an X-ray source, generating either diethylammonium ($C_4H_{12}N^+$) or nitrate ($^{15}NO_3^-$) ions. Nitrogen flows over DEA and $H^{15}NO_3$ samples were at 10 ml min^{-1} and 50 ml min^{-1} respectively. In an electric field, the primary ion (or reagent ion) is guided towards the 10 L min^{-1} sample flow, where ionization occurs via clustering with sampled molecules. The resulting charged clusters are directed through a critical orifice into an atmospheric pressure interface time-of-flight mass spectrometer (APi-TOF), where they are detected based on mass-to-charge ratios (m/z) (Junninen et al., 2010). For quantification of CIMS data, the concentration of the molecule X is defined as

$$[X] = C \times \frac{X\ ion\ signals}{reagent\ ion\ signals} \quad (S2)$$

In the case of $H^{15}NO_3$ and DEA, the equations are shown as follows

$$[X] = C \times \frac{X \cdot \left(\sum_{j=0}^{1}\sum_{i=0}^{1-j}(HNO_3)_i \cdot (H^{15}NO_3)_j \cdot NO_3^- + \sum_{j=0}^{1}(H^{15}NO_3)_j \cdot {}^{15}NO_3^-\right)}{\sum_{j=0}^{2}\sum_{i=0}^{2-j}(HNO_3)_i \cdot (H^{15}NO_3)_j \cdot NO_3^- + \sum_{j=0}^{2}(H^{15}NO_3)_j \cdot {}^{15}NO_3^-} \quad (S3)$$

$$[X] = C \times \frac{X \cdot C_4H_{12}N^+}{C_4H_{12}N^+ + C_4H_{11}N \cdot C_4H_{12}N^+} \quad (S4)$$

The numerators in equations S3 and S4 are the measured signal intensities of the molecule X clustered by primary ions. In nitrate mode, we saw monomer (e.g., $^{15}NO_3^-$) or dimer (e.g., $H^{15}NO_3 \cdot {}^{15}NO_3^-$) charged clusters, while in DEA mode, we mostly saw monomer (i.e., $C_4H_{12}N^+$) charged ones. Note that in nitrate mode, we also observed adduct products with ^{14}N nitrates, which were also included in equation S3. This occurred because the NO_2 cylinder also produced HNO_3 into our setup. Nevertheless, the ^{15}N-labeled reagent ions consistently dominated the ionization pathways for the detected products in all experiments. The denominator in both equations (S3 and S4) corresponds to the total signal intensity of reagent ions. A calibration factor (C) is required to convert normalized signals to concentrations. Due to lack of an independent synthesis route for generation of RO_2 radicals and closed-shell products, a calibration factor of 7.3×10^9 cm^{-3} (± 50%) was estimated from the sulfuric acid calibration experiments (He et al., 2023; Kürten et al., 2012). This approach has also been applied and validated in previous studies (Berndt et al., 2018, 2025), but possible differences in mass transmission of the instruments can cause additional uncertainties for larger organic molecules.

The Vocus proton-transfer-reaction time-of-flight mass spectrometer (Vocus PTR-TOF, Tofwerk AG) consists of two main components: the Vocus chemical ionization source and a standard time-of-flight mass spectrometer (HTOF). The Vocus consists of a discharge reagent-ion source and a focusing ion-molecule reactor (FIMR), for use in PTR-TOF measurements of volatile organic compounds (VOCs) (Krechmer et al., 2018). The reagent-ion source uses a low-pressure discharge to produce hydronium ions (H_3O^+), which are directed into the FIMR. Sample air enters the FIMR through a short (10 mm) PEEK tube with an internal diameter of 0.18 mm, acting as a pressure restriction similar to a critical orifice. VOCs in the sample air are ionized via proton-transfer-reactions and then detected by the HTOF. Further instrumental details are available in Krechmer et al. (2018). Calibration was performed using a gas-phase standard from a calibration cylinder (Apel-Riemer Environmental, Inc.) containing 19 VOC components, including α-pinene (AP). The sensitivity of AP was approximately 781 cps ppb^{-1}. When the syringe pump system was set to deliver 80 ppb of AP, the Vocus PTR-TOF measured 84 ppb, confirming the accuracy of the syringe pump system. Since the proton-transfer rate constants between hydronium ions and different monoterpenes are quite similar (Zhao and Zhang, 2004), we expect the initial MT concentrations to have an uncertainty of no more than about 20%. This syringe pump system was also used to inject other four MTs and TME at specific rates based on target concentrations.

The concentrations of NO_2 and O_3 were measured by gas monitors. A photometric O_3 analyzer (model 400, Teledyne API) was used to detect O_3 in the free-jet flow-tube. The amount of O_3 determines how much of a 254 nm UV light signal is absorbed in the sample cell. The absorption difference between the intact sample air and the O_3-removed air, achieved by a switching valve periodically, enables the determination of the stable O_3 concentrations. NO_2 was measured using an NO–NO_2 analyzer (model T200UP, Teledyne API). With a high-efficiency photolytic converter, NO_2 is transformed to NO with minimal interference from other gases. Using the chemiluminescence detection principle, NO is measured by reacting with O_3, yielding light in direct proportion to the amount of NO (Archer et al., 1995). In this way, both sampled NO and total NO_x can be measured, without and with using the photolytic converter, respectively. This enables the determination of the NO_2 concentration in the sample by subtraction.

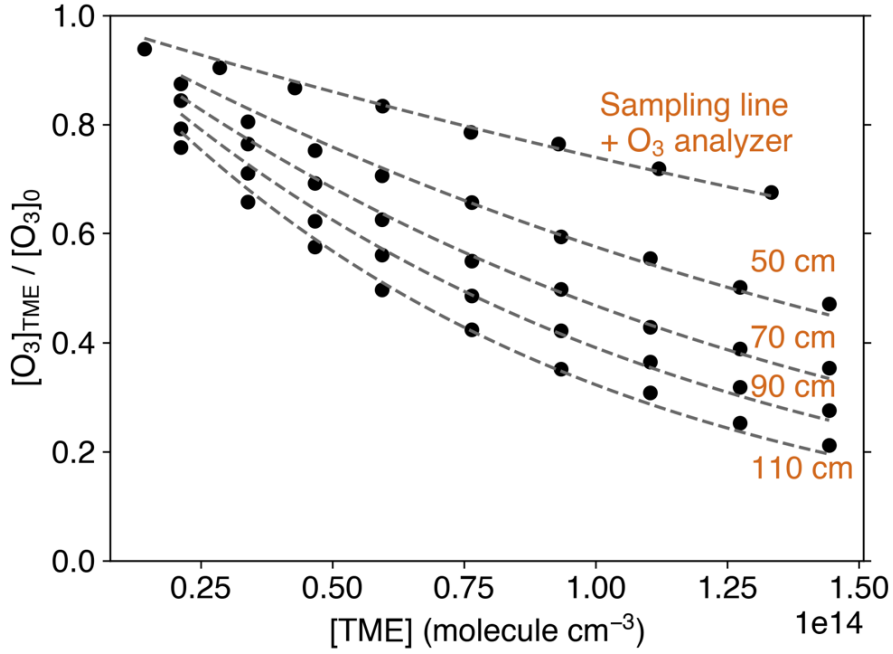

Figure S1. Determination of the reaction time for different reaction distances between the nozzle and the sampling port (50 – 110 cm) by measuring the decay of O_3 from its reaction with excessive TME: 2.5 s (50 cm), 4.6 s (70 cm), 6.4 s (90 cm), and 8.3 s (110 cm). Details see Section S1.

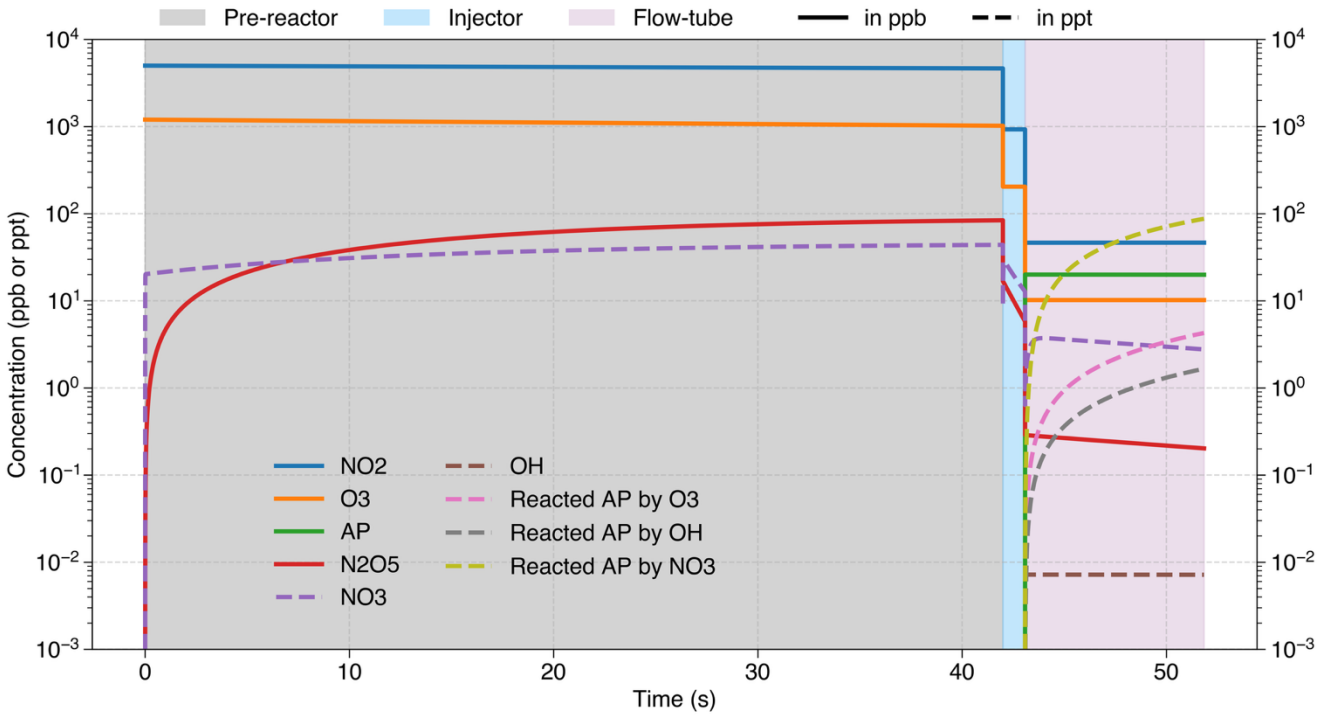

Figure S2. Time series of modeled compounds in the experiment with initial concentrations (in 100 L min^{-1}) of AP, O_3, and NO_2 at 20, 12, and 50 ppb (stage 6 in Fig. 2). In the pre-reactor (total flow: 1 L min^{-1}), initial concentrations of O_3, and NO_2 are 1200 and 5000 ppb. The reaction times are: 42 s (pre-reactor), 1.086 s (injector), and 8.8 s (flow-tube including the sampling inlet).

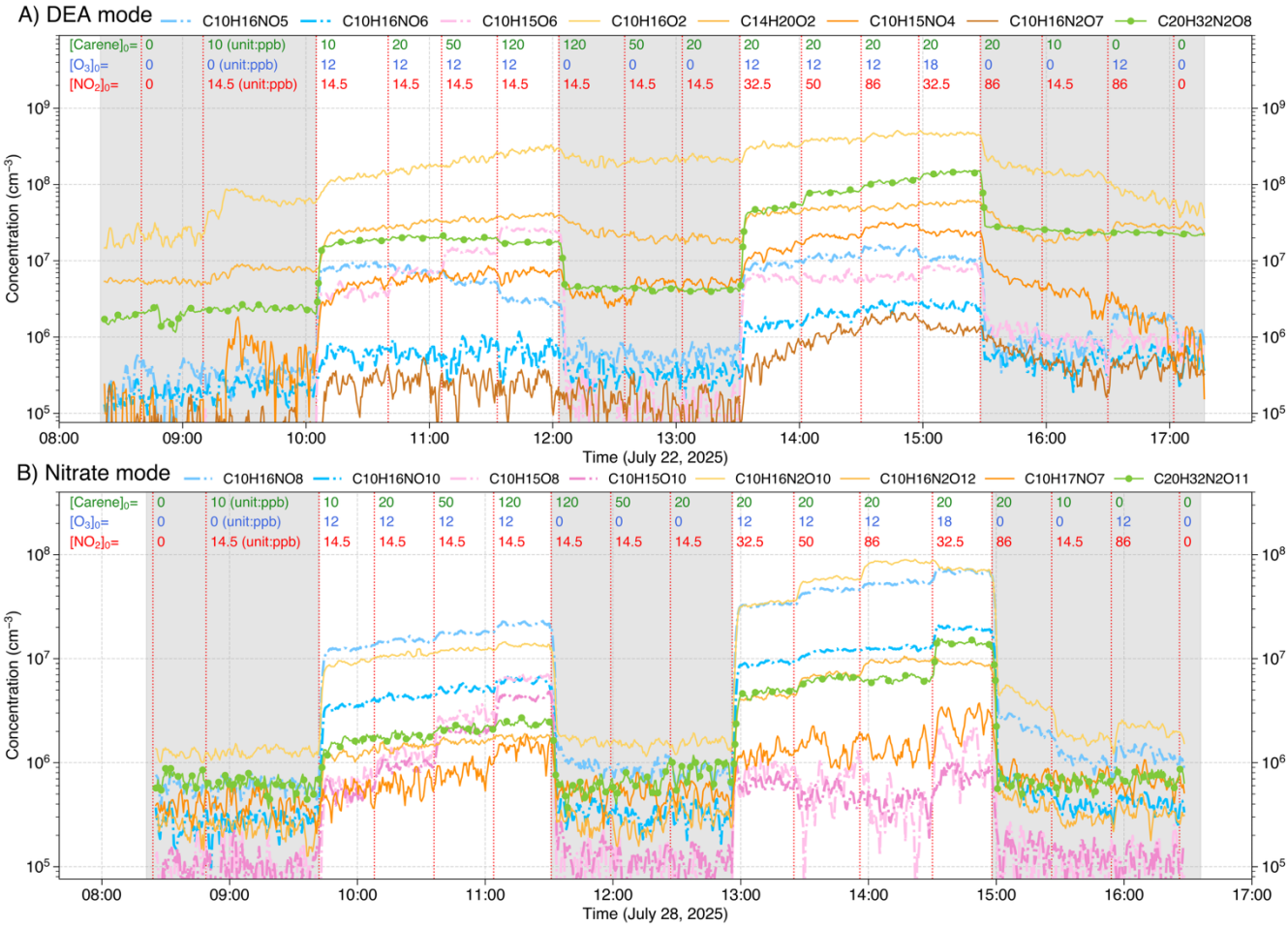

Figure S3. Timeseries of major products from Δ-3-carene + NO_3 experiments measured using both DEA (panel A) and nitrate (panel B) modes. Concentrations (in cm^{-3}) of radicals, closed-shell monomers, and closed-shell dimers are shown as dash-dot lines, solid lines, and solid lines with markers, respectively. Products are color-coded by origin: expected NO_3 oxidation products (radicals, closed-shell monomers, and dimers) are shown in blue, yellow-orange, and green colors, respectively, while expected O_3/OH oxidation products are shown in pink. Grey shaded areas represent background stages. Initial precursor concentrations (in ppb) shown above each subplot correspond to values present in the total flow of 100 L min^{-1}, without any chemical conversion. The effective reaction time is 8.8 s.

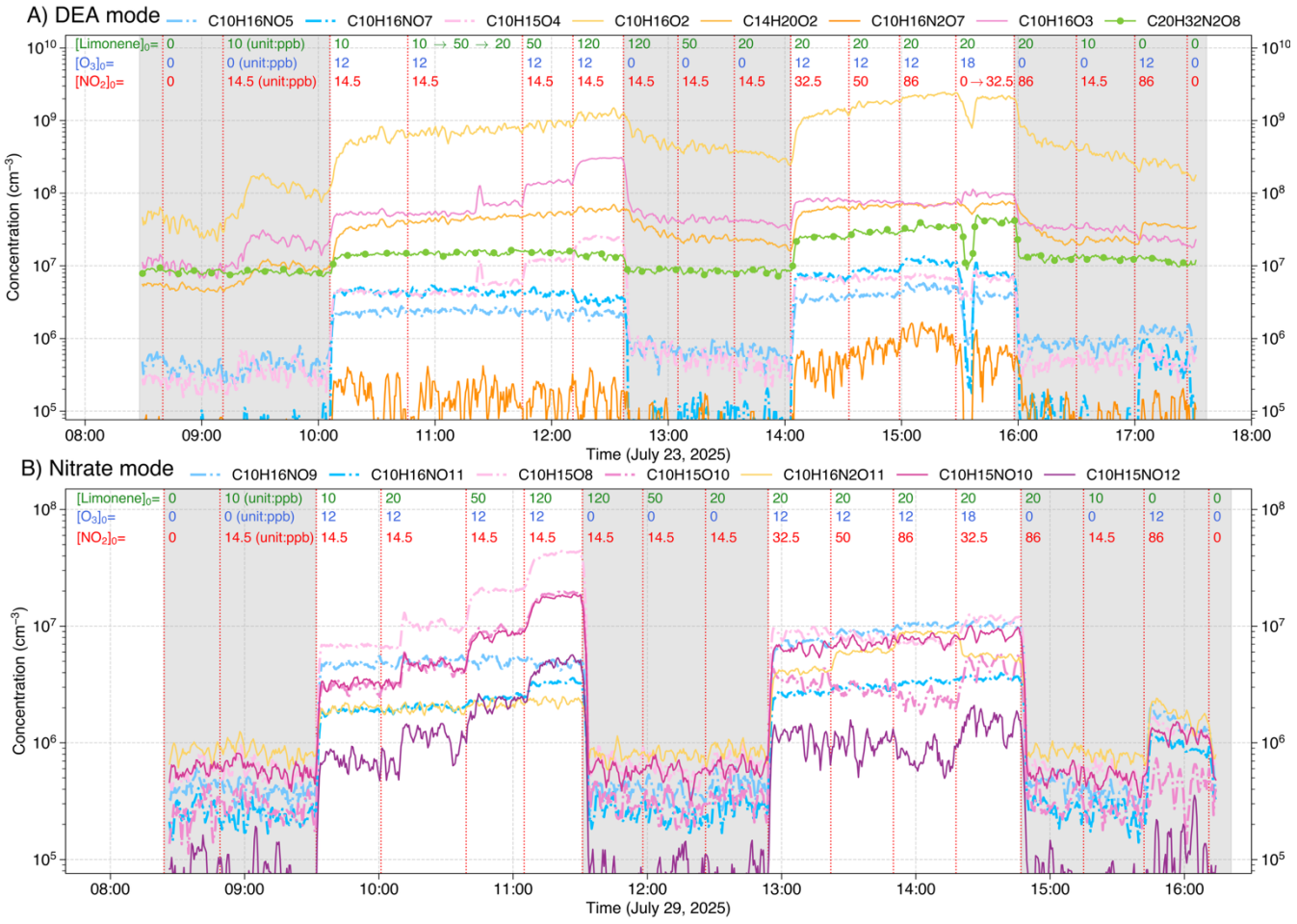

Figure S4. Timeseries of major products from limonene + NO_3 experiments measured using both DEA (panel A) and nitrate (panel B) modes. Concentrations (in cm^{-3}) of radicals, closed-shell monomers, and closed-shell dimers are shown as dash-dot lines, solid lines, and solid lines with markers, respectively. Products are color-coded by origin: expected NO_3 oxidation products (radicals, closed-shell monomers, and dimers) are shown in blue, yellow-orange, and green colors, respectively, while expected O_3/OH oxidation products are shown in pink. Grey shaded areas represent background stages. Initial precursor concentrations (in ppb) shown above each subplot correspond to values present in the total flow of 100 L min^{-1}, without any chemical conversion. The effective reaction time is 8.8 s.

Figure S5. Timeseries of major products from β-pinene (BP) + NO_3 experiments measured using both DEA (panel A) and nitrate (panel B) modes. Concentrations (in cm^{-3}) of radicals, closed-shell monomers, and closed-shell dimers are shown as dash-dot lines, solid lines, and solid lines with markers, respectively. Products are color-coded by origin: expected NO_3 oxidation products (radicals, closed-shell monomers, and dimers) are shown in blue, yellow-orange, and green colors, respectively, while expected O_3/OH oxidation products are shown in pink. Grey shaded areas represent background stages. Initial precursor concentrations (in ppb) shown above each subplot correspond to values present in the total flow of 100 L min^{-1}, without any chemical conversion. The effective reaction time is 8.8 s.

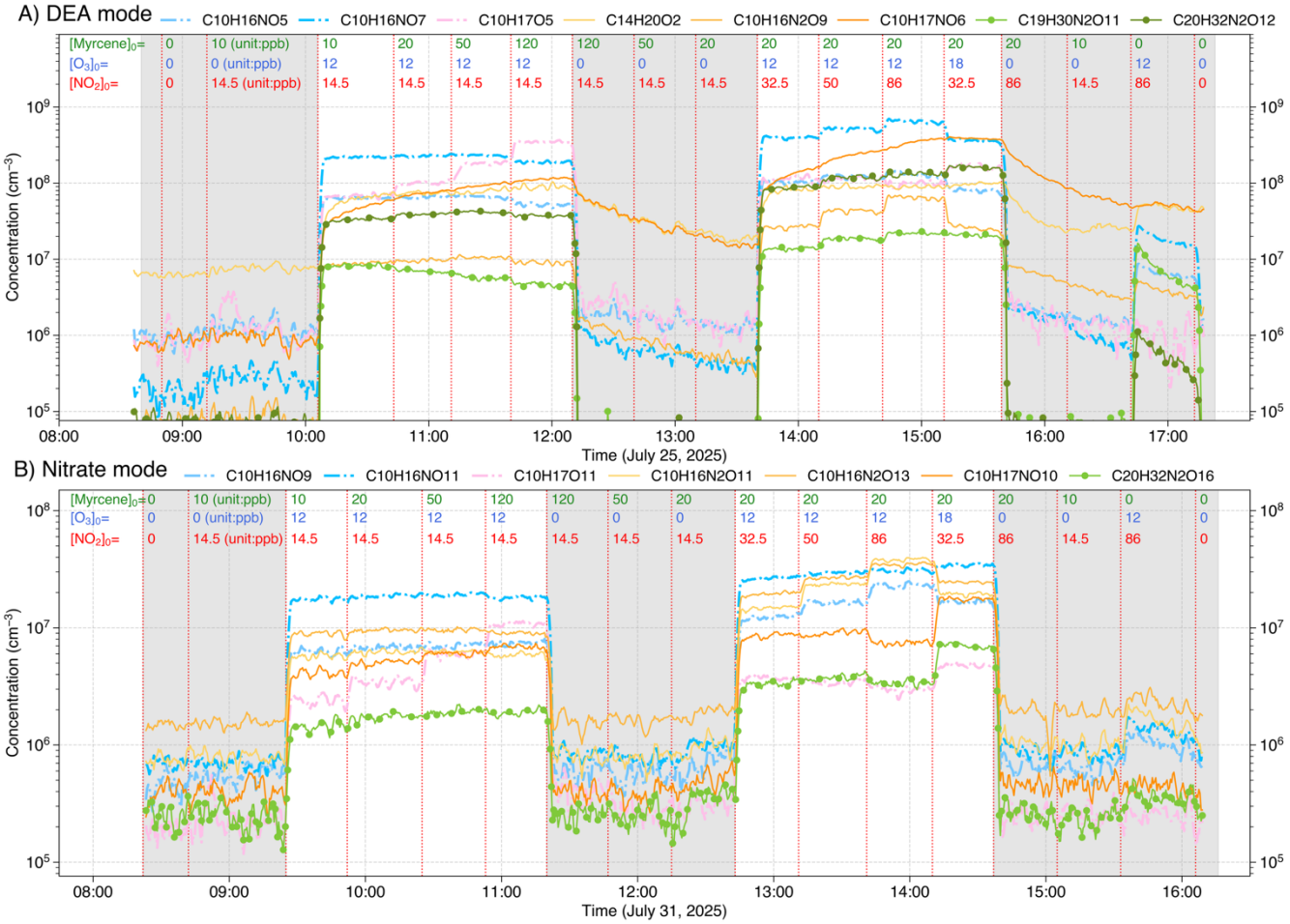

Figure S6. Timeseries of major products from β-myrcene + NO_3 experiments measured using both DEA (panel A) and nitrate (panel B) modes. Concentrations (in cm^{-3}) of radicals, closed-shell monomers, and closed-shell dimers are shown as dash-dot lines, solid lines, and solid lines with markers, respectively. Products are color-coded by origin: expected NO_3 oxidation products (radicals, closed-shell monomers, and dimers) are shown in blue, yellow-orange, and green colors, respectively, while expected O_3/OH oxidation products are shown in pink. Grey shaded areas represent background stages. Initial precursor concentrations (in ppb) shown above each subplot correspond to values present in the total flow of 100 L min^{-1}, without any chemical conversion. The effective reaction time is 8.8 s.

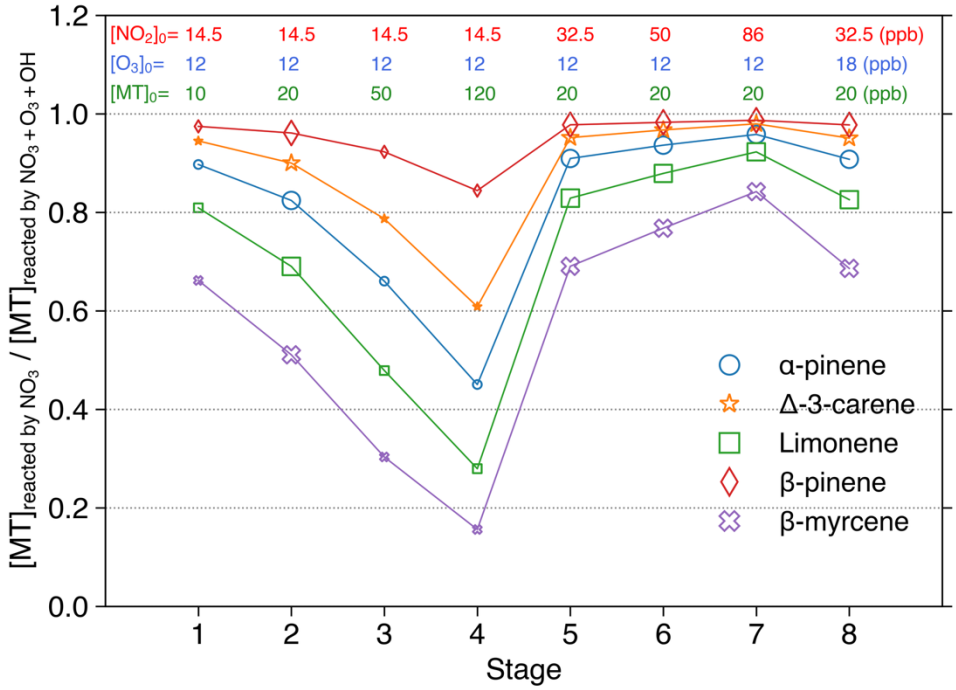

135 **Figure S7. Ratio of reacted [MT] by NO_3 to total reacted [MT] by NO_3, O_3, and OH, as a function of experimental stage. Different marker shapes and colors represent different MTs. Initial precursor concentrations (in ppb) shown above each subplot correspond to values present in the total flow of 100 L min^{-1}, without any chemical conversion. Stages 2, 5, 6, 7, and 8 (indicated by larger markers) were selected for studying NO_3 oxidation products, as these stages have a constant initial MT concentration of 20 ppb while systematically varying the NO_2/O_3 conditions.**

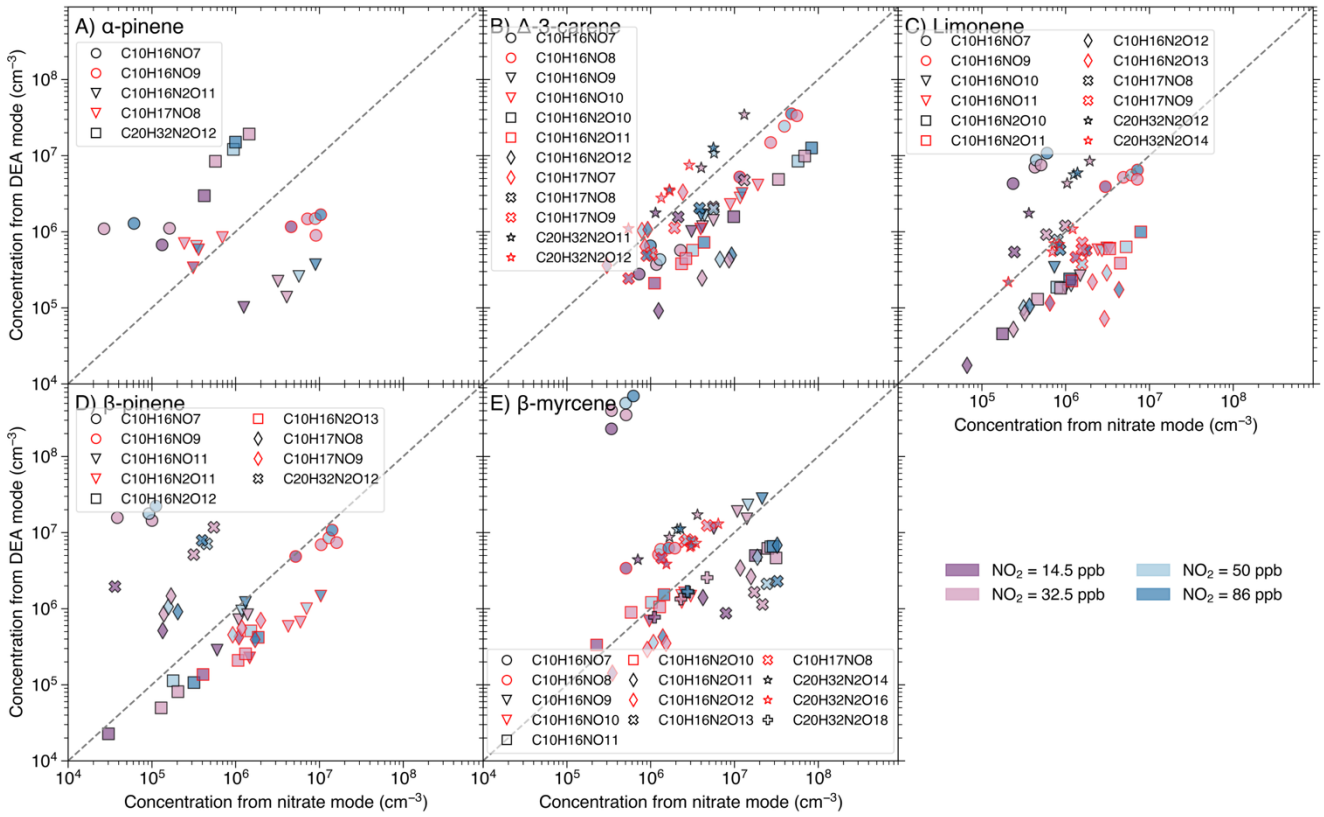

140

Figure S8. The comparison of major NO_3 oxidation product (monomers with O ≥ 7, dimers with O ≥ 11, and peroxynitrates with O ≥ 10) concentrations from both DEA and nitrate mode. The marker face colors indicate the initial NO_2 levels of experimental stages while shapes and edge colors indicate individual compounds.

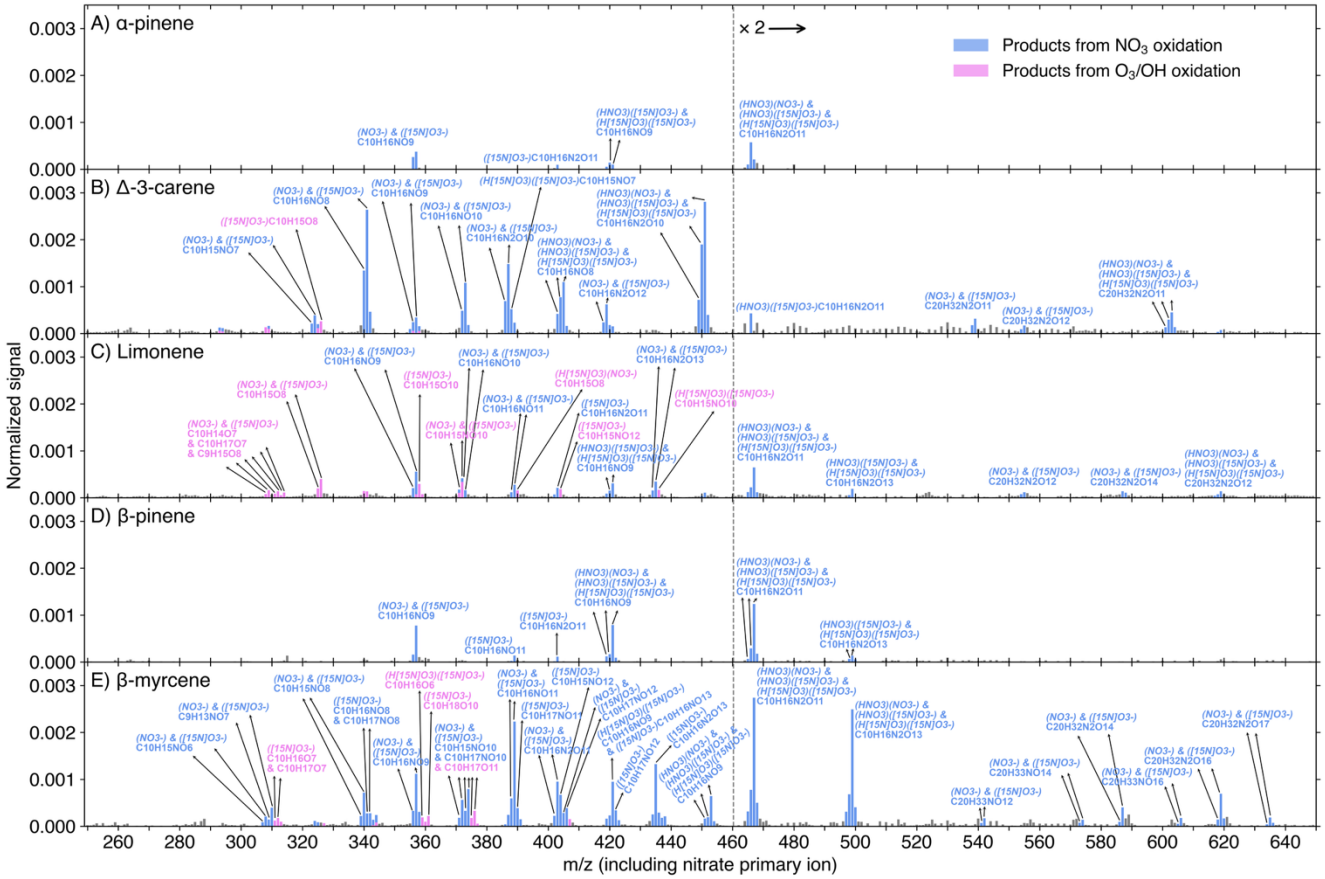

145 **Figure S9. Nitrate-CIMS spectra (10 min average) of MT + NO_3 reactions at the experimental stage 6, with detailed charging schemes displayed in the parentheses. Initial concentrations were $[MT]_0$ = 20 ppb, $[O_3]_0$ = 12 ppb, and $[NO_2]_0$ = 50 ppb, with an effective reaction time of 8.8 s. The spectra display the normalized peak signals (see Equation S3) and were corrected by subtracting background signals. Blue bars represent products (including both radicals and closed-shell species) from NO_3 oxidation, pink bars show products from O_3 or OH oxidation, and grey bars are for peaks not of interest. Peaks larger than 460 Th are multiplied by 2.**

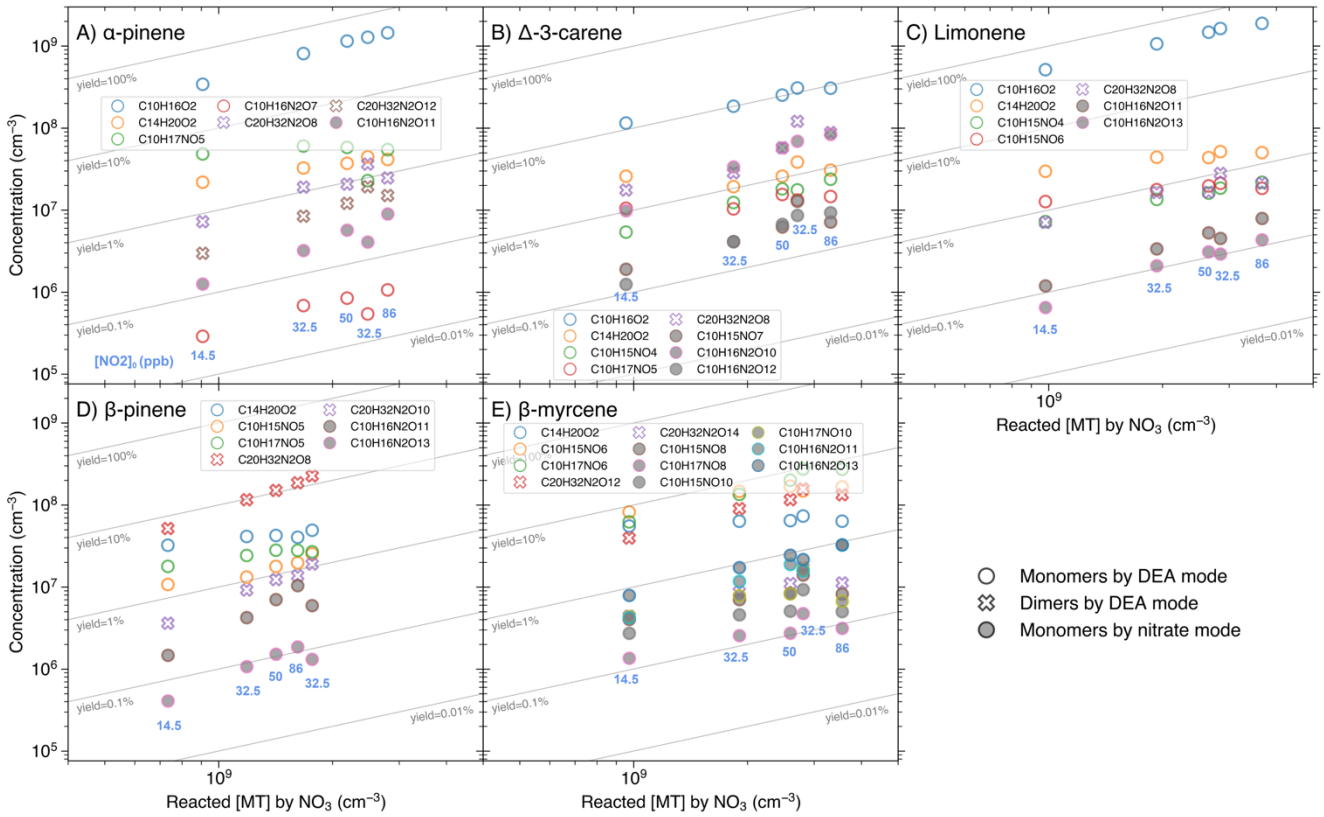

Figure S10. Concentrations (in cm^{-3}) of the major closed-shell products from the MTs + NO_3 reaction, as a function of reacted [MT] by the NO_3 radical. Data from experimental stages 2 and 5–8 are presented as 10 min averaged measurements taken at an effective reaction time of 8.8 s. The reacted [MT] by NO_3 was varied primarily by increasing $[NO_2]_0$ (values in ppb shown beneath each column). The only exception is the transition from stage 7 to stage 8, where $[O_3]_0$ increased from 12 to 18 ppb and $[NO_2]_0$ decreased from 86 to 34.5 ppb (see Fig. 2). Circles represent monomers measured by the DEA mode, crosses represent dimers measured by the DEA mode, and filled circles represent monomers by the nitrate mode.

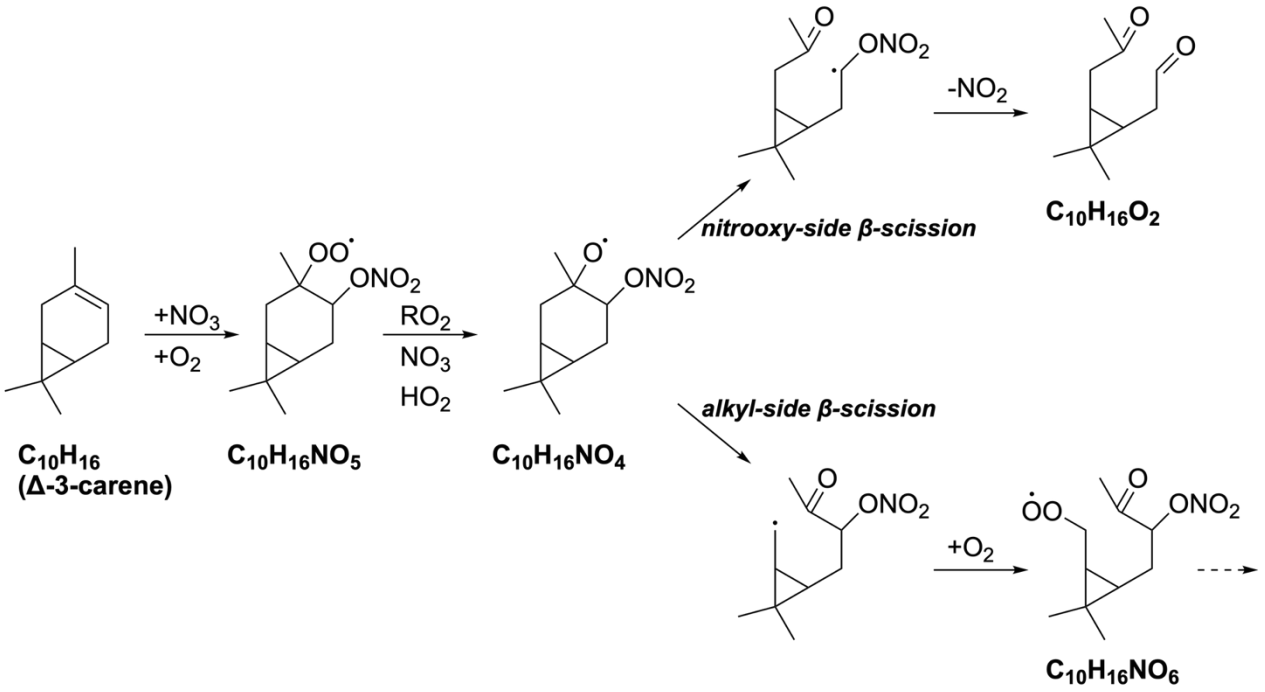

Figure S11. Schematic showing two competing RO scission pathways of the nitrooxy alkoxy radical, $C_{10}H_{16}NO_4$, originating from the Δ-3-carene + NO_3 reaction. The nitrooxy-side β-scission leads to the formation of $C_{10}H_{16}O_2$ while the alkyl-side β-scission promotes further autoxidation (Draper et al., 2019; Kurtén et al., 2017). The RO scission pathways for α-pinene and limonene follow the same pattern.

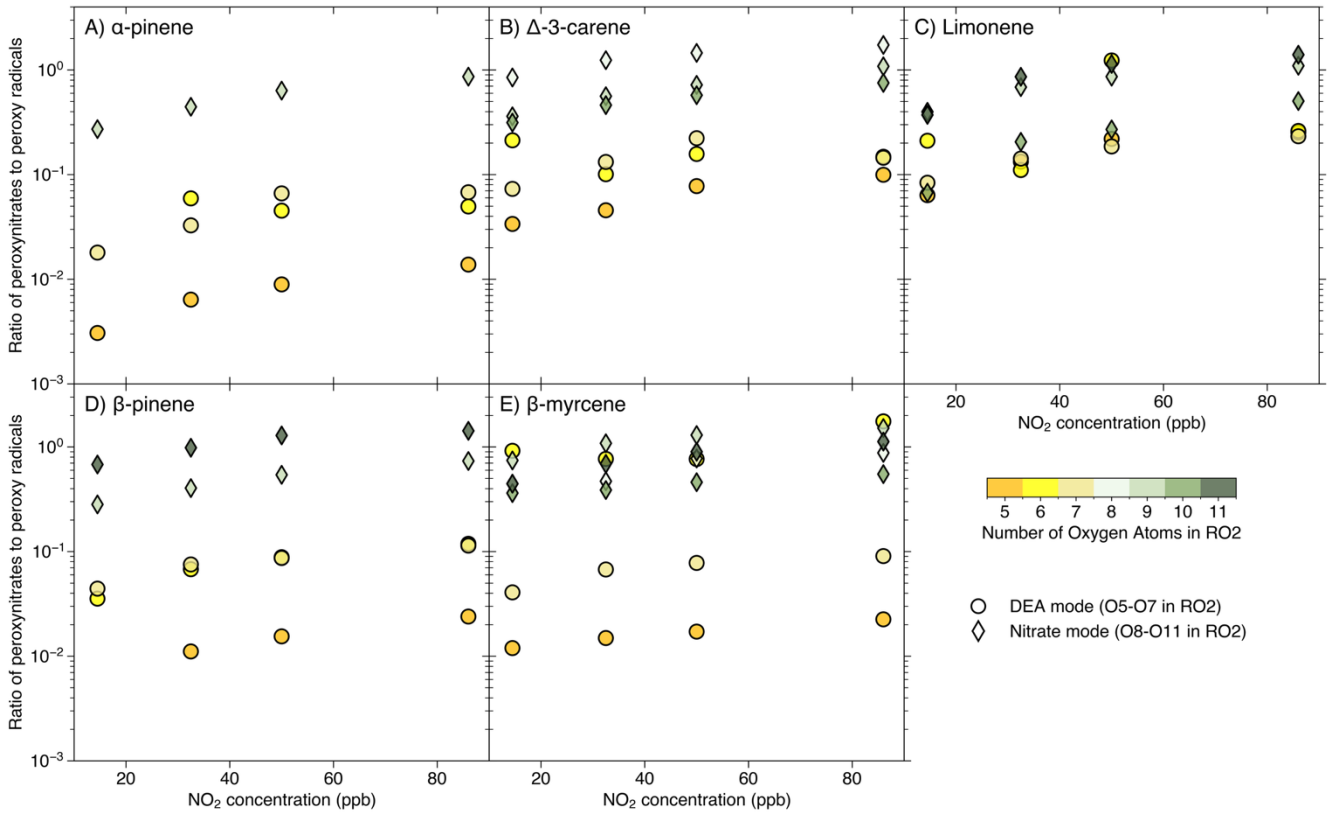

Figure S12. Ratio of peroxynitrates (RO_2NO_2) to their parent peroxy radicals (RO_2), as a function of initial NO_2 concentration ($[NO_2]_0$). Data from experimental stages 2 and 5–7 are presented as 10 min averaged measurements taken at an effective reaction time of 8.8 s. The RO_2 radicals with O = 5 to 7 and their corresponding RO_2NO_2 are measured from the DEA mode (their ratio presented in circles), while RO_2 with O = 8 to 11 and their RO_2NO_2 are measured from the nitrate mode (their ratio presented in diamonds). Data points are colored according to the number of oxygen atoms in the parent RO_2 radical.

Table S1. Reactions and their reaction rate coefficients used for the box model describing the flow-tube experiments. Rate coefficients at 298 ± 2 K were taken from literature or estimated based on reported values.

Reactions	Rate coefficients[a]	Reference
Alpha-pinene + NO_3 → products	6.2×10^{-12}	(Atkinson et al., 1984; Barnes et al., 1990)
Delta-3-Carene + NO_3 → products	9.1×10^{-12}	
Limonene + NO_3 → products	1.2×10^{-11}	
Beta-pinene + NO_3 → products	2.5×10^{-12}	
Myrcene + NO_3 → products	1.1×10^{-11}	(Atkinson et al., 1984; Martínez et al., 1999)
Alpha-pinene + O_3 → 0.8 × OH + products	9.6×10^{-17}	(Aschmann et al., 2002; Atkinson et al., 1990, 1992; Bernard et al., 2012; Witter et al., 2002)
Delta-3-Carene + O_3 → 0.86 × OH + products	4.9×10^{-17}	
Limonene + O_3 → 0.66 × OH + products	2.2×10^{-16}	
Beta-pinene + O_3 → 0.3 × OH + products	1.9×10^{-17}	
Myrcene + O_3 → 0.63 × OH + products	4.7×10^{-16}	
Alpha-pinene + OH → products	5.3×10^{-11}	(Atkinson et al., 1986; Gill and Hites, 2002)
Limonene + OH → products	1.6×10^{-10}	
Beta-pinene + OH → products	7.6×10^{-11}	
Delta-3-Carene + OH → products	9×10^{-11}	(Atkinson et al., 1986; Grosjean and Williams, 1992)
Myrcene + OH → products	2.2×10^{-10}	(Atkinson et al., 1986; Tan et al., 2021)
$NO_2 + O_3 \rightarrow NO_3 + O_2$	3.2×10^{-17}	(Atkinson et al., 2004; Ghormley et al., 1973)
$NO_3 + NO_2 \rightarrow N_2O_5$	1.9×10^{-12}	(Atkinson et al., 2004)
$N_2O_5 \rightarrow NO_3 + NO_2$	0.07	
$NO_3 + OH \rightarrow NO_2 + HO_2$	2×10^{-11}	
$O_3 + OH \rightarrow O_2 + HO_2$	7.3×10^{-14}	
$NO_2 + OH \rightarrow HNO_3$	2.4×10^{-11}	(D'Ottone et al., 2001)
NO_3 → Wall (inner diameter: 4 cm)	0.1	(Lambe et al., 2020)
NO_3 → Wall (inner diameter: 8 mm)	0.24	
N_2O_5 → Wall (inner diameter: 4 cm)	0.04	
N_2O_5 → Wall (inner diameter: 8 mm)	1	

[a] Units: cm^3 $molecule^{-1}$ s^{-1} (bimolecular reactions) or s^{-1} (unimolecular reactions).

Reference

Archer, S. L., Shultz, P. J., Warren, J. B., Hampl, V., and DeMaster, E. G.: Preparation of Standards and Measurement of Nitric Oxide, Nitroxyl, and Related Oxidation Products, Methods, 7, 21–34, https://doi.org/10.1006/meth.1995.1004, 1995.

Aschmann, S. M., Arey, J., and Atkinson, R.: OH radical formation from the gas-phase reactions of O_3 with a series of terpenes, Atmos. Environ., 36, 4347–4355, https://doi.org/10.1016/S1352-2310(02)00355-2, 2002.

Atkinson, R., Plum, C. N., Carter, W. P. L., Winer, A. M., and Pitts, J. N. Jr.: Rate constants for the gas-phase reactions of nitrate radicals with a series of organics in air at 298 .+-. 1 K, J. Phys. Chem., 88, 1210–1215, https://doi.org/10.1021/j150650a039, 1984.

Atkinson, R., Aschmann, S. M., and Pitts, J. N.: Rate constants for the gas-phase reactions of the OH radical with a series of monoterpenes at 294 ± 1 K, Int. J. Chem. Kinet., 18, 287–299, https://doi.org/10.1002/kin.550180303, 1986.

Atkinson, R., Hasegawa, D., and Aschmann, S. M.: Rate constants for the gas-phase reactions of O_3 with a series of monoterpenes and related compounds at 296 ± 2 K, Int. J. Chem. Kinet., 22, 871–887, https://doi.org/10.1002/kin.550220807, 1990.

Atkinson, R., Aschmann, S. M., Arey, J., and Shorees, B.: Formation of OH radicals in the gas phase reactions of O_3 with a series of terpenes, J. Geophys. Res. Atmos., 97, 6065–6073, https://doi.org/10.1029/92JD00062, 1992.

Atkinson, R., Baulch, D. L., Cox, R. A., Crowley, J. N., Hampson, R. F., Hynes, R. G., Jenkin, M. E., Rossi, M. J., and Troe, J.: Evaluated kinetic and photochemical data for atmospheric chemistry: Volume I - gas phase reactions of O_x, HO_x, NO_x and SO_x species, Atmos. Chem. Phys., 4, 1461–1738, https://doi.org/10.5194/acp-4-1461-2004, 2004.

Barnes, Ian., Bastian, Volker., Becker, K. H., and Tong, Zhu.: Kinetics and products of the reactions of nitrate radical with monoalkenes, dialkenes, and monoterpenes, J. Phys. Chem., 94, 2413–2419, https://doi.org/10.1021/j100369a041, 1990.

Bernard, F., Fedioun, I., Peyroux, F., Quilgars, A., Daële, V., and Mellouki, A.: Thresholds of secondary organic aerosol formation by ozonolysis of monoterpenes measured in a laminar flow aerosol reactor, J. Aerosol Sci., 43, 14–30, https://doi.org/10.1016/j.jaerosci.2011.08.005, 2012.

Berndt, T., Richters, S., Kaethner, R., Voigtländer, J., Stratmann, F., Sipilä, M., Kulmala, M., and Herrmann, H.: Gas-Phase Ozonolysis of Cycloalkenes: Formation of Highly Oxidized RO_2 Radicals and Their Reactions with NO, NO_2, SO_2, and Other RO_2 Radicals, J. Phys. Chem. A, 119, 10336–10348, https://doi.org/10.1021/acs.jpca.5b07295, 2015a.

Berndt, T., Kaethner, R., Voigtländer, J., Stratmann, F., Pfeifle, M., Reichle, P., Sipilä, M., Kulmala, M., and Olzmann, M.: Kinetics of the unimolecular reaction of CH_2OO and the bimolecular reactions with the water monomer, acetaldehyde and acetone under atmospheric conditions, Phys. Chem. Chem. Phys., 17, 19862–19873, https://doi.org/10.1039/C5CP02224J, 2015b.

Berndt, T., Richters, S., Jokinen, T., Hyttinen, N., Kurtén, T., Otkjær, R. V., Kjaergaard, H. G., Stratmann, F., Herrmann, H., Sipilä, M., Kulmala, M., and Ehn, M.: Hydroxyl radical-induced formation of highly oxidized organic compounds, Nat. Commun., 7, 13677, https://doi.org/10.1038/ncomms13677, 2016.

Berndt, T., Mentler, B., Scholz, W., Fischer, L., Herrmann, H., Kulmala, M., and Hansel, A.: Accretion Product Formation from Ozonolysis and OH Radical Reaction of α-Pinene: Mechanistic Insight and the Influence of Isoprene and Ethylene, Environ. Sci. Technol., 52, 11069–11077, https://doi.org/10.1021/acs.est.8b02210, 2018.

Berndt, T., Hoffmann, E. H., Tilgner, A., and Herrmann, H.: Highly oxidized products from the atmospheric reaction of hydroxyl radicals with isoprene, Nat. Commun., 16, 2068, https://doi.org/10.1038/s41467-025-57336-1, 2025.

D'Ottone, L., Campuzano-Jost, P., Bauer, D., and Hynes, A. J.: A Pulsed Laser Photolysis−Pulsed Laser Induced Fluorescence Study of the Kinetics of the Gas-Phase Reaction of OH with NO_2, J. Phys. Chem. A, 105, 10538–10543, https://doi.org/10.1021/jp012250n, 2001.

Draper, D. C., Myllys, N., Hyttinen, N., Møller, K. H., Kjaergaard, H. G., Fry, J. L., Smith, J. N., and Kurtén, T.: Formation of Highly Oxidized Molecules from NO_3 Radical Initiated Oxidation of Δ-3-Carene: A Mechanistic Study, ACS Earth Space Chem., 3, 1460–1470, https://doi.org/10.1021/acsearthspacechem.9b00143, 2019.

Eisele, F. L. and Tanner, D. J.: Measurement of the gas phase concentration of H_2SO_4 and methane sulfonic acid and estimates of H_2SO_4 production and loss in the atmosphere, J. Geophys. Res., 98, 9001–9010, https://doi.org/10.1029/93JD00031, 1993.

Ghormley, J. A., Ellsworth, R. L., and Hochanadel, C. J.: Reaction of excited oxygen atoms with nitrous oxide. Rate constants for reaction of ozone with nitric oxide and with nitrogen dioxide, J. Phys. Chem., 77, 1341–1345, https://doi.org/10.1021/j100630a005, 1973.

Gill, K. J. and Hites, R. A.: Rate Constants for the Gas-Phase Reactions of the Hydroxyl Radical with Isoprene, α- and β-Pinene, and Limonene as a Function of Temperature, J. Phys. Chem. A, 106, 2538–2544, https://doi.org/10.1021/jp013532q, 2002.

Grosjean, D. and Williams, E. L.: Environmental persistence of organic compounds estimated from structure-reactivity and linear free-energy relationships. Unsaturated aliphatics, Atmos. Environ. Part A, 26, 1395–1405, https://doi.org/10.1016/0960-1686(92)90124-4, 1992.

He, X.-C., Shen, J., Iyer, S., Juuti, P., Zhang, J., Koirala, M., Kytökari, M. M., Worsnop, D. R., Rissanen, M., Kulmala, M., Maier, N. M., Mikkilä, J., Sipilä, M., and Kangasluoma, J.: Characterisation of gaseous iodine species detection using the multi-scheme chemical ionisation inlet 2 with bromide and nitrate chemical ionisation methods, Atmos. Meas. Tech., 16, 4461–4487, https://doi.org/10.5194/amt-16-4461-2023, 2023.

Junninen, H., Ehn, M., Petäjä, T., Luosujärvi, L., Kotiaho, T., Kostiainen, R., Rohner, U., Gonin, M., Fuhrer, K., Kulmala, M., and Worsnop, D. R.: A high-resolution mass spectrometer to measure atmospheric ion composition, Atmos. Meas. Tech., 3, 1039–1053, https://doi.org/10.5194/amt-3-1039-2010, 2010.

Krechmer, J., Lopez-Hilfiker, F., Koss, A., Hutterli, M., Stoermer, C., Deming, B., Kimmel, J., Warneke, C., Holzinger, R., Jayne, J., Worsnop, D., Fuhrer, K., Gonin, M., and de Gouw, J.: Evaluation of a New Reagent-Ion Source and Focusing Ion–Molecule Reactor for Use in Proton-Transfer-Reaction Mass Spectrometry, Anal. Chem., 90, 12011–12018, https://doi.org/10.1021/acs.analchem.8b02641, 2018.

Kürten, A., Rondo, L., Ehrhart, S., and Curtius, J.: Calibration of a Chemical Ionization Mass Spectrometer for the Measurement of Gaseous Sulfuric Acid, J. Phys. Chem. A, 116, 6375–6386, https://doi.org/10.1021/jp212123n, 2012.

Kurtén, T., Møller, K. H., Nguyen, T. B., Schwantes, R. H., Misztal, P. K., Su, L., Wennberg, P. O., Fry, J. L., and Kjaergaard, H. G.: Alkoxy Radical Bond Scissions Explain the Anomalously Low Secondary Organic Aerosol and Organonitrate Yields From α-Pinene + NO_3, J. Phys. Chem. Lett., 8, 2826–2834, https://doi.org/10.1021/acs.jpclett.7b01038, 2017.

Lambe, A. T., Wood, E. C., Krechmer, J. E., Majluf, F., Williams, L. R., Croteau, P. L., Cirtog, M., Féron, A., Petit, J.-E., Albinet, A., Jimenez, J. L., and Peng, Z.: Nitrate radical generation via continuous generation of dinitrogen pentoxide in a

laminar flow reactor coupled to an oxidation flow reactor, Atmos. Meas. Tech., 13, 2397–2411, https://doi.org/10.5194/amt-13-2397-2020, 2020.

Martínez, E., Cabañas, B., Aranda, A., Martín, P., and Salgado, S.: Absolute Rate Coefficients for the Gas-Phase Reactions of NO_3 Radical with a Series of Monoterpenes at T = 298 to 433 K, J. Atmos. Chem., 33, 265–282, https://doi.org/10.1023/A:1006178530211, 1999.

Tan, Z., Hantschke, L., Kaminski, M., Acir, I.-H., Bohn, B., Cho, C., Dorn, H.-P., Li, X., Novelli, A., Nehr, S., Rohrer, F., Tillmann, R., Wegener, R., Hofzumahaus, A., Kiendler-Scharr, A., Wahner, A., and Fuchs, H.: Atmospheric photo-oxidation of myrcene: OH reaction rate constant, gas-phase oxidation products and radical budgets, Atmos. Chem. Phys., 21, 16067–16091, https://doi.org/10.5194/acp-21-16067-2021, 2021.

Witter, M., Berndt, T., Böge, O., Stratmann, F., and Heintzenberg, J.: Gas-phase ozonolysis: Rate coefficients for a series of terpenes and rate coefficients and OH yields for 2-methyl-2-butene and 2,3-dimethyl-2-butene, Int. J. Chem. Kinet., 34, 394–403, https://doi.org/10.1002/kin.10063, 2002.

Zhang, J., Zhang, Y., Koskenvaara, H., Zhao, J., and Ehn, M.: Dataset for article “Gas-phase products from nitrate radical oxidation of five monoterpenes: insights from free-jet flow-tube experiments,” Zenodo [data set] [dataset], https://doi.org/10.5281/zenodo.17250833, 2025.

Zhao, J. and Zhang, R.: Proton transfer reaction rate constants between hydronium ion (H_3O^+) and volatile organic compounds, Atmos. Environ., 38, 2177–2185, https://doi.org/10.1016/j.atmosenv.2004.01.019, 2004.